ELSEVIER

Medical Image Analysis 7 (2003) 47–64

MEDICAL IMAGE ANALYSIS

www.elsevier.com/locate/media

Irregularity index: A new border irregularity measure for cutaneous melanocytic lesions

Tim K. Lee[a,b,*], David I. McLean[c,d], M. Stella Atkins[b]

[a]*Cancer Control Research Program, BC Cancer Agency, Vancouver, BC, Canada V5Z 4E6*
[b]*School of Computing Science, Simon Fraser University, Burnaby, BC, Canada V5A 1S6*
[c]*Divisions of Dermatology, Vancouver Hospital and Health Sciences Centre and the University of British Columbia, Vancouver, BC, Canada V5Z-4E8*
[d]*Division of Dermatology, BC Cancer Agency, Vancouver, BC, Canada V5Z 4E6*

Received 12 July 2000; received in revised form 11 November 2001; accepted 18 April 2002

Abstract

One of the important clinical features that differentiates benign melanocytic nevi from malignant melanomas is the irregularity of the lesion border. There are two types of border irregularities: texture irregularities, the small variations along the border, and structure irregularities, the global indentations and protrusions. Texture irregularities are subject to noise, whereas structure irregularities may suggest excessive cell growth or regression of a melanoma. We have designed a new algorithm for measuring the structure irregularities in the border. Our algorithm first locates all the local and global indentations and protrusions and organizes them in a hierarchical structure. Then an area-based index, called the irregularity index, is computed for each indentation and protrusion along the border. From the individual irregularity indices, two important new measures, the most significant irregularity index and the overall irregularity index are derived. These two new indices provide a measure of the degree of irregularity along the lesion border. A double-blinded test was performed to examine the effectiveness of these two new indices. Fourteen experienced dermatologists were asked to evaluate the borders of 40 pigmented lesions. The clinical evaluation result was then compared with the two new indices and other published shape measurements. The user study showed that both of the new indices vastly outperformed the other shape descriptors. Moreover, our algorithm captured the knowledge of expert dermatologists in analysing malignancy of a lesion based on its shape alone, indicating that the new measures may be useful for diagnosing melanomas.

Keywords: Melanoma; Border irregularity; Shape descriptor; Scale space filtering

1. Introduction

Cutaneous melanocytic lesions are the common brown pigmented skin lesions known as moles. These lesions are formed by nests of specialized cells called melanocytes in the outer layer of the skin. Melanocytes produce a pigment called melanin, which protects the body from harmful ultraviolet radiation. When melanocytes proliferate, a skin lesion is formed and a pigmented mark appears. The majority of such pigmented skin lesions are benign, medically known as melanocytic nevi; however, some of the lesions are malignant, medically known as cutaneous malignant melanomas. Early diagnosis of malignant melanomas is crucial to treatment processes because the survival rate is inversely proportional to the thickness of the lesion (Balch et al., 1989). Due to the increasing incidence rate in the last three decades (Armstrong and English, 1996), many dermatologists are searching for non-invasive computer-aided diagnostic systems which can help health care providers to diagnose early lesions and to improve diagnostic accuracy and consistency. Furthermore, such a diagnostic device can reduce the number of skin biopsies (Stoecker and Moss, 1992; Hall et al., 1995; Fleming, 2000).

*Corresponding author. Tel.: +1-604-707-5922; fax: +1-604-877-1868.
E-mail address: tlee@bccancer.bc.ca (T.K. Lee).

1361-8415/02/$ – see front matter
PII: S1361-8415(02)00090-7

Studies have been conducted to investigate the possibility of detecting melanomas using image analysis techniques. The clinical surface view features (border irregularity, asymmetry, texture, colour and lesion size) and clinical subsurface view features (pigment networks, brown globules, black dots, radial streaming and pseudopods) have been extracted and analysed (Cascinelli et al., 1987; White et al., 1991, 1992; Schindewolf et al., 1992; Binder et al., 1994; Ercal et al., 1994; Hall et al., 1995; Seidenari et al., 1995; Gutkowicz-Krusin et al., 1997; Menzies et al., 1997; Colot et al., 1998; Fleming, 2000). These features were often extracted from colour images, but wide spectrum images including invisible wavelengths have also been investigated (Cotton et al., 1999; Bono et al., 1999; Elbaum, 2000). Based on an optical model of skin, Cotton et al. (1999) was able to derive features such as the amount of dermal blood and epidermal melanin from colour and near-infrared images. Although the above features (surface view or subsurface view, structure-based or texture-based) provide important evidence for melanoma, none of them can provide a proper diagnosis by itself. A classifier is required to analyse *all* features to generate a diagnosis.

Among all features, lesion shape is one of the important symptoms for diagnosing melanoma. Clinically, benign nevi are often described as small skin lesions with uniform colour. They usually have a round or oval shape border. On the other hand, malignant melanomas usually appear as enlarged nevi with multiple shades of colours, and their borders tend to be irregular and asymmetric with protrusions and indentations (Maize and Ackerman, 1987; Rivers, 1996). Fig. 1 shows a typical benign nevus (Fig. 1(a)) and a malignant melanoma (Fig. 1(b)). Among these melanoma features, border irregularity has been reported as the most significant factor in clinical diagnosis (Keefe et al., 1990). Histologically, protrusions along the lesion border may suggest abnormality and excessive cell growth in a sub-population of the melanocytes, while indentations may suggest an occurrence of regression in the melanoma. Therefore, marked border irregularities may be indicative of malignancy of a pigmented skin lesion. In this paper, we concentrate on how to measure border irregularity effectively so that the measurement can be used as an input feature by a classifier for malignant melanomas.

1.1. Types of border irregularities

When a lesion border is studied carefully, we notice two types of irregularities: texture and structure irregularities (Claridge et al., 1992). Texture irregularities are the fine variations along the lesion border. Detecting and measuring texture irregularities may be subject to noise from the hardware imaging devices and/or software programs. On the contrary, structure irregularities, which are general undulations of the perimeter, may infer the abnormal histological signs discussed in the previous section, and have a higher correlation with melanomas (Claridge et al., 1992). Therefore, measuring structure irregularities accurately is important for diagnosing melanomas. Fig. 2 shows both types of irregularities with three border outlines extracted from pigmented skin lesions. Lesion border A has no structure protrusion and indentation, but a lot of texture irregularities. Lesion border B has a structure protrusion at the top of the border but has less texture

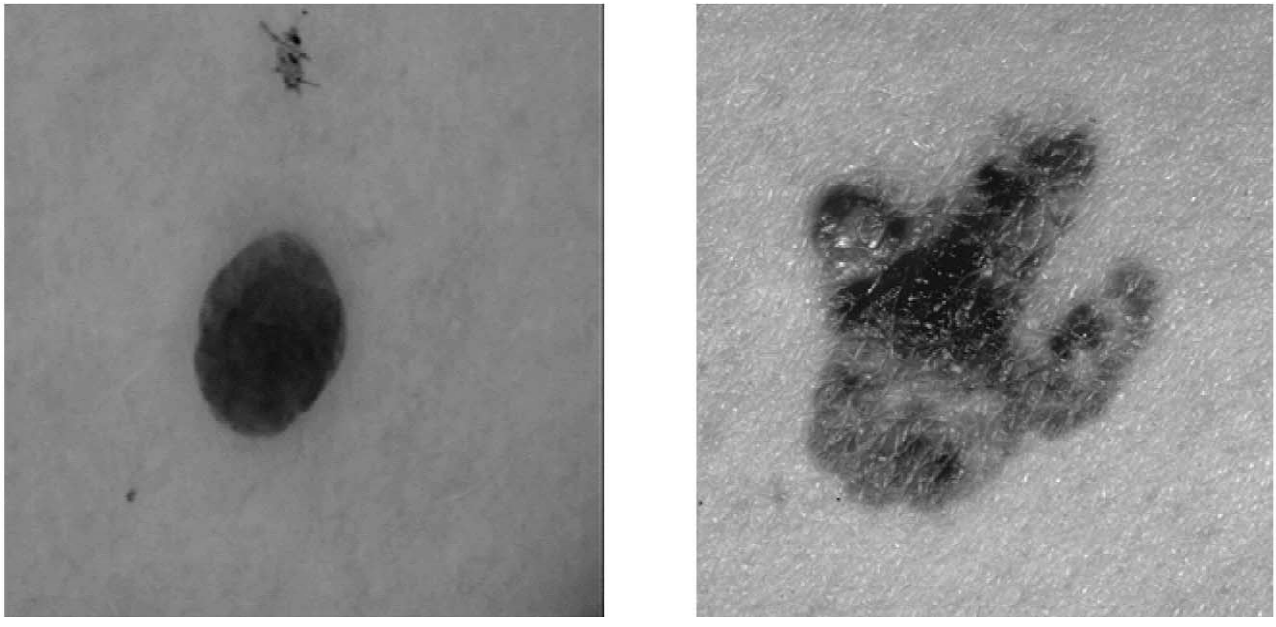

(a) (b)

Fig. 1. Melanocytic lesions: (a) Benign nevus; (b) Malignant melanoma.

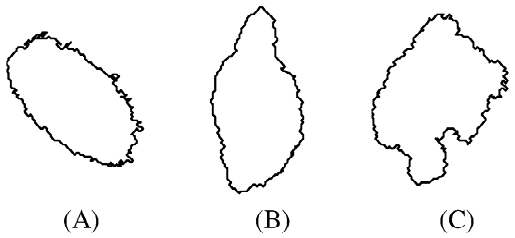

Fig. 2. Three lesion borders.

irregularity than the other two borders, while lesion border C has a prominent structure protrusion and indentation at the bottom of the border.

1.2. Previous work

Most previous studies used some common shape descriptors such as the compactness index (CI) (White et al., 1992; Golston et al., 1992; Ercal et al., 1994; Stoecker et al., 1995; Colot et al., 1998) or the fractal dimension (FD) (Claridge et al., 1992, 1998; Hall et al., 1995; Ng and Lee, 1996) to measure border irregularity. Unfortunately, the CI is sensitive to noise along the border. Alternatively, Mandelbrot's FD (Mandelbrot, 1982) has been used extensively to measure the roughness (jaggedness) of a border or a surface for many applications (Pentland, 1984; MacAulay, 1989; Caldwell et al., 1990; Chaudhuri and Sarkar, 1995). However, the FD does not measure structure irregularities. In an attempt to capture major structural features, Claridge et al. (1992) designed a measure called Structure Fractal Dimension (SFD), where the lesion border is smoothed slightly before the FD is computed. There are problems with this measure which we discuss later in Section 4.2.

In our earlier work, we reported a new measure for border irregularity, called Sigma-Ratio (SR) (Lee et al., 1999), which is based on the number of Gaussian smoothing iterations required for eliminating all concavities along the lesion border. We showed that this simple index is more sensitive to structure indentation and protrusion than the CI, FD and SFD. However, there are some shortcomings of the SR measure. First, the SR measure is non-linear. Second, the SR measure is sensitive to a long and narrow indentation such as the one shown in Fig. 3(a). When an occluding hair of a skin lesion is misinterpreted as a long and narrow indentation by a pre-processing segmentation program, the lesion border has a high SR, which can be similar to the SR of a much larger indentation as shown in Fig. 3(b). Hence, using the SR measure requires all hairs to be removed carefully either by shaving, or by using a pre-processing program such as DullRazor (Lee et al., 1997).

1.3. Structure of the paper

In this paper, we extend the SR measure to two new area-based measurements, called the most significant irregularity index (MSII) and the overall irregularity index (OII), by directly locating and measuring indentations and protrusions along the lesion border so that the resulting measure is sensitive to structure irregularities. To examine the effectiveness of these new measurements, we performed a user study with fourteen experienced dermatologists by comparing their clinical evaluations of forty lesion borders against the MSII, OII, CI, FD and SFD.

In Section 2, we describe the algorithm for our new measures in detail. Section 3 describes our user study with expert dermatologists. Section 4 discusses the results and Section 5 concludes with a summary and further work.

2. Algorithm for irregularity index

2.1. Preprocessing lesion images

The original skin lesion images are automatically preprocessed by two programs to extract the lesion border

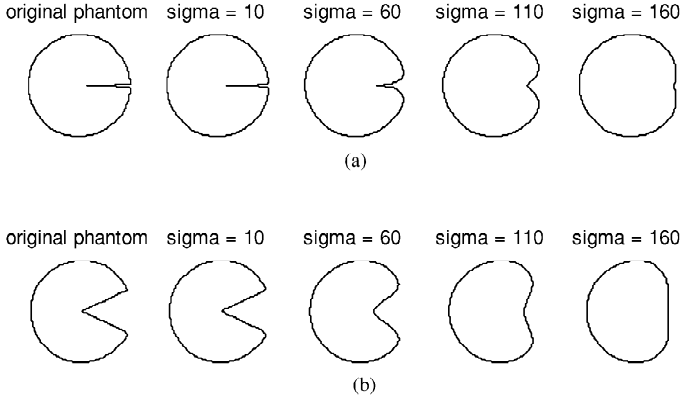

Fig. 3. Phantoms for the sigma-ratio: (a) A small indentation that is long and narrow; (b) a large indentation. Both phantoms are smoothed by Gaussian kernels with an increasing Gaussian σ, which is reported at the top of the smoothed border. Since both phantoms require a similar amount of smoothing, in term of Gaussian σ, to eliminate all concavities on the border, they have a similar sigma-ratio in spite of the different indentation sizes.

contour. First, the skin image is screened for dark thick hairs. These hairs are removed by a software program called DullRazor (Lee et al., 1997) to reduce hair interference on the subsequent automated segmentation program. Then the lesion border contour is extracted automatically (Lee et al., 1995). Fig. 2 shows three of the extracted lesion borders.

2.2. Abstraction of lesion border

In order to analyse indentations and protrusions along a lesion border, we abstract the border as a planar curve L_0. Further simplification can be made by parameterization of the x and y coordinates into two linear functions $x(t)$ and $y(t)$, where $0 \leqslant t \leqslant 1$ is the path length variable along the planar curve,

$$L_0 = (x(t), y(t)). \tag{1}$$

The initial point of the parameterization, $t = 0$, can be selected arbitrarily; however, the border is traced in the counterclockwise direction so that the interior of the lesion is in the left-hand side of the border during the tracking process. Furthermore, $L_0(x(0), y(0)) = L_0(x(1), y(1))$, because the border forms a closed contour.

2.3. Partition border into indentation and protrusion segments

A simple method to measure irregularities (indentations and protrusions) along a curve is to compute the corresponding curvature function. For any curve $L(x(t), y(t))$, the curvature function $K(t)$ can be computed as (Greenspan and Benney, 1973)

$$K(t) = \frac{\frac{\mathrm{d}x}{\mathrm{d}t}\frac{\mathrm{d}^2y}{\mathrm{d}t^2} - \frac{\mathrm{d}y}{\mathrm{d}t}\frac{\mathrm{d}^2x}{\mathrm{d}t^2}}{\left(\left(\frac{\mathrm{d}x}{\mathrm{d}t}\right)^2 + \left(\frac{\mathrm{d}y}{\mathrm{d}t}\right)^2\right)^{2/3}}. \tag{2}$$

With our convention, using counterclockwise tracing along the border and image coordinate system[1], positive curvature values imply concavity, while negative curvature values imply convexity. Local curvature extrema, located by the zero-crossings of the first derivative of $K(t)$, mark the tip points of concave and convex segments. These tip points are considered to have high information content (Attneave, 1954) and have been frequently used to partition border contours into parts. Hoffman and Richards (Hoffman and Richards, 1985; Richards and Hoffman, 1985; Richards et al., 1986) partitioned object borders at concave tips and their part primitives, codons, are constituted of curve segments with 0, 1 or 2 curvature extrema. Siddiqi and Kimia's (Siddiqi and Kimia, 1995) neck-based and limb-based approach for object decomposition also put the terminals of part-lines at the concave tips. These partition rules produce only protrusion segments.

We too exploit local curvature extrema to divide the border into a set of indentation/protrusion segments which are defined as curve segments composed of three consecutive local curvature extrema $[t_1, t_2, t_3]$, where t_1, t_2 and t_3 are specified by the path length variables of the curve. The middle curvature extremum t_2 denotes the segment tip point and the segment type. For example, when t_2 is a concave curvature extremum, $K(t_2) > 0$, the corresponding segment is an indentation segment. Otherwise, a convex curvature extremum t_2, $K(t_2) < 0$, specifies a protrusion segment. The local curvature extrema t_1 and t_3 delineate the extent of the segment and they have a different sign from curvature extremum t_2,

$$\begin{aligned} &\mathrm{sign}(K(t_1)) = \mathrm{sign}(K(t_3)), \\ &\mathrm{sign}(K(t_1)) \neq \mathrm{sign}(K(t_2)). \end{aligned} \tag{3}$$

In other words, an indentation segment is defined as a curve segment that begins with a convex curvature extremum, followed by a concave curvature extremum and a convex curvature extremum. Similarly, a protrusion segment, defined as a dual of an indentation, is a curve segment that begins with a concave curvature extremum, followed by a convex curvature extremum and a concave extremum. In Fig. 4, a curve segment with overlapping protrusions and indentations is shown. The points B, D and F specify the tips of the protrusion segments and the points A, C, E and G specify the tip of the indentation segments. The corresponding curvature function is also plotted. The local curvature extrema, points A to G, are determined by the zero-crossings of the first derivative of the curvature function, $\mathrm{d}(K)/\mathrm{d}t$. By applying the definition of indentation/protrusion segments, we can locate the indentation segments as the curve segments [B, C, D] and [D, E, F] and the protrusion segments as [A, B, C], [C, D, E] and [E,

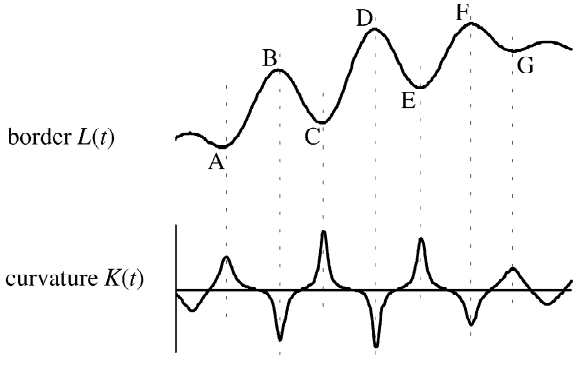

Fig. 4. Definition for indentations and protrusions. The border $L(t)$ depicts a portion of the object border. The interior of the object is below the line. The curvature $K(t)$ shows the corresponding curvature function. The points A, C, E and G are the concave curvature extrema, while the points B, D and F are the convex curvature extrema.

[1]The original is in the top-left corner.

F, G]. Therefore, a lesion border can be decomposed into a set of indentation/protrusion segments by scanning the corresponding curvature function for three consecutive curvature extrema with alternating signs.

2.4. Extract structure indentation and protrusion segments

2.4.1. Scale dependence of irregularity segments

Computing indentation/protrusion segments using the method described in Section 2.3 is scale dependent and brings up a question: what is the optimal scale for structural indentation/protrusion segments? One answer is to use several pre-defined scales. However, this approach has problems of selecting appropriate scales and relating information found among scales. We use a well-known method called the scale-space filtering technique, which provides a solution for scale selection and information passing in a multi-scale environment (Witkin, 1983; Asada and Brady, 1983; Richards et al., 1986; Lindeberg, 1993, 1994; Mokhtarian and Mackworth, 1986; Mokhtarian and Suomela, 1998).

2.4.2. Classic curvature scale-space filtering

The idea of classic curvature scale-space filtering (Mokhtarian and Mackworth, 1986; Mokhtarian and Suomela, 1998) is based on the smoothing process of the original border function $L_0(x(t), y(t))$ by convolving $x(t)$ and $y(t)$ with a Gaussian kernel $g(t, r)$ of increasing width,

$$L(t, \sigma) = L_0(x(t), y(t)) \otimes g(t, \sigma), \tag{4}$$

$$= (X(t, \sigma), Y(t, \sigma)), \tag{5}$$

where $L(t, \sigma)$ is the smoothed border and $\otimes$ denotes the convolution operator and

$$X(t, \sigma) = x(t) \otimes g(t, \sigma), \quad Y(t, \sigma) = y(t) \otimes g(t, \sigma) \tag{6}$$

and

$$g(t, \sigma) = \frac{1}{\sigma\sqrt{2\pi}} e^{-t^2/2\sigma^2}. \tag{7}$$

The Gaussian standard deviation σ controls the amount of smoothing and the smoothing process is terminated at σ_{term} when all concavities of the border are removed. The smoothing process is demonstrated in both Figs. 3 and 5. In Fig. 5, using the lesion border C of Fig. 2, the smoothing process terminates at $\sigma_{\text{term}} = 129$.

The scale-space filtering technique proposes a binary 2D scale-space image to record the zero curvature locations for the entire smoothing process (see Fig. 6(a)). The classic curvature scale-space image is often referred to as a binary image, because only two values are needed to display the zero curvature points in contrast to the background. The y-axis of the image represents the smoothing scale, denoted by Gaussian σ, while the x-axis represents the path length variable t, which specifies the spatial positions of zero curvature points satisfying $K(t, \sigma) = 0$ and $\partial K(t, \sigma)/\partial t \neq 0$.

2.4.3. Extended curvature scale-space filtering

The classic curvature scale-space filtering has been used successfully to represent the shape of planar curves in object recognition systems; however, the technique was

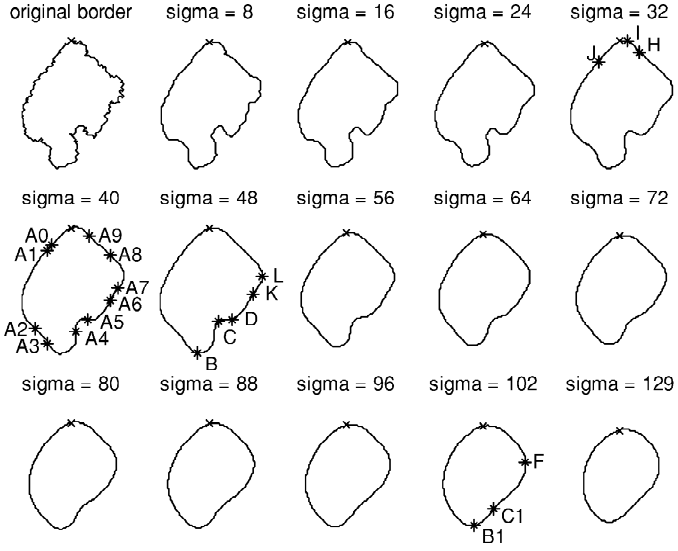

Fig. 5. Gaussian smoothing process of the lesion border C shown in Fig. 2. Only some of the smoothing levels, specified at the top of each subfigure, are plotted. The parameterization of the closed curves begins at the point marked as 'x' and the parameterization is done in the counterclockwise direction. At $\sigma = 40$, all points with zero curvature value are marked as '*' and also shown in Fig. 6(a). The protrusion segment [H, I, J] at $\sigma = 32$, and the indentation segments [B, C, D] and [B1, C1, F] at $\sigma = 48$ and 102, respectively, are also shown in Fig. 6(b). The segment [H, I, J] wraps around the initial point of the parameterization process.

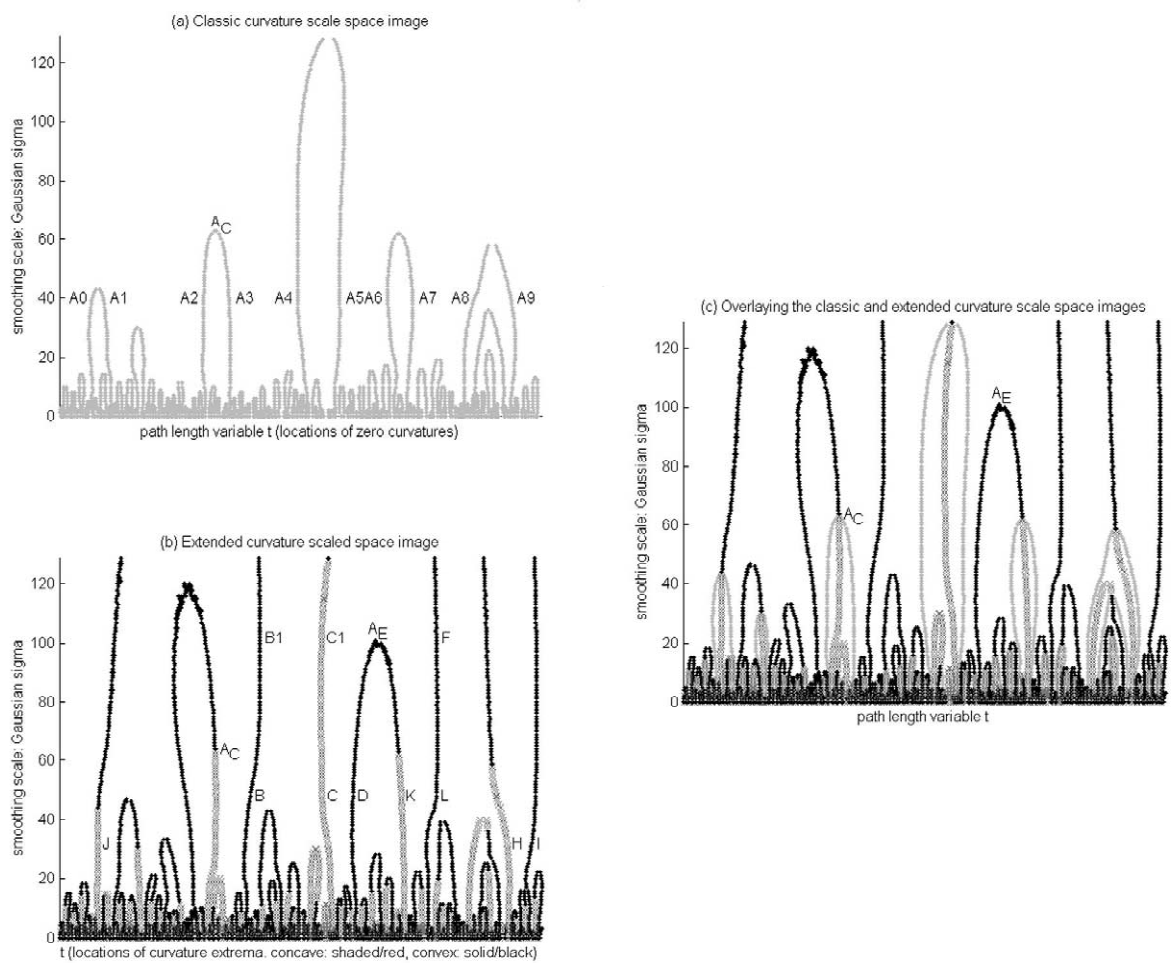

Fig. 6. The classic (a) and extended (b) curvature scale-space images for the Gaussian smoothing process shown in Fig. 5. (c) The overlay of (a) and (b).

not designed to analyse indentation and protrusion segments as defined in Section 2.3. We modified the classic technique, in order to investigate the locations of curvature extrema, which are the zero-crossings of the partial derivative of $K(t, r)$ with respect to t, i.e.,

$$\frac{\partial K(t,\sigma)}{\partial t} = 0, \quad \frac{\partial^2 K(t,\sigma)}{\partial t^2} \neq 0. \tag{8}$$

Because we keep track of the locations of the convex and concave curvature extrema, our extended curvature scale-space image is considered as a 3-valued image.[2] To construct such an extended image, the zero-crossings of the first derivative of the curvature function for each smoothing scale σ are determined and their positions are recorded on the image along with their concavity or convexity property. For example, Fig. 6(b) depicts the extended scale-space image for the smoothing process shown in Fig. 5. The curvature extrema B, C and D at $\sigma = 48$ in Fig. 5 are recorded as points B, C and D in Fig. 6(b). The concavity property of C (in shaded thick point or in red for the colour version) and the convexity property of B and D (in black solid points) are also marked accordingly. In other words, the extended scale-space image captures all indentation/protrusion segments for the entire smoothing process. To reveal these segments at each smoothing level, we scan for three consecutive curvature extrema with alternating signs (colours) sequentially from σ_{term} to $\sigma = 0$, the original non-smoothed curve.

There are similarities and differences between the classic and our extended curvature scale-space images. A comparison of the mathematical properties of both scale-space images is summarized in Appendix A and is detailed with proofs in (Lee et al., 2001). Both images show many contour arcs formed by the loci of the respective investigated features, which are selected based on the purpose of the process: the classic process is designed to represent the object shape, while the extended process is designed to investigate all indentation and protrusion segments along the border. Mathematically, these loci are related and form

[2]The extended curvature scale-space image is considered as a three-valued image because it requires 3 values to encode the concave curvature extrema, the convex curvature extrema and the background, whereas classic curvature scale-space images are often referred as binary images.

a dual space. Graphically, the comparison can be made by overlaying the images as in Fig. 6(c).

Because the initial border, $\sigma = 0$, is sampled and represented in discrete space, the curvature value computation for the initial border is not very accurate. However, we are interested in only the curvature extrema locations, whose estimation should be reasonably accurate. Furthermore, the length of the border shrinks during the smoothing process. The border is no longer represented by discrete values after a few iterations. Hence, the concern of computational accuracy for derivatives and curvature values is eliminated.

For some extreme shapes, such as a comb-like shape with long narrow teeth (Fig. 7), the curve may self-intersect during the smoothing process. Parameterizing the smoothed border by arc-length at each iteration overcomes this problem (Gage and Hamilton, 1986; Grayson, 1987; ter Haar Romeny, 1994). However, the re-sampling de-emphasizes the shape differences at fine scales (Mokhtarian and Mackworth, 1992). For our practical application of analysing skin lesion border, lesion borders are most unlikely to have such an extreme shape. Furthermore, the border is most likely to have uniform noise, so we followed the recommendation of Mokhtarian and Mackworth (1992) and we did not opt for arc length evolution. During our experiments with lesion borders described in detail in the next section, we did not observe the self-intersection problem with any of our lesion borders.

2.4.4. Evolution of indentation/protrusion segments

As an indentation/protrusion segment evolves through the smoothing process, the segment may span several scales. Unfortunately, Gaussian smoothing distorts the contour length and, hence, the location of indentation/protrusion segments shifts from scale to scale. Matching up the segments between scales becomes a difficult task. The extended scale-space image facilitates the matching by analysing the loci formed by the curvature extrema points. For example, tracking the convex extrema lines B and D of the indentation segment [B, C, D] at $\sigma = 48$ of Fig. 6(b) toward the zero-scale reveals the *true* position of the segment of the original non-smoothed curve at $\sigma = 0$. The tracking of extrema lines is achieved in the following manner. Points, the curvature extrema, at σ_{term} are first detected. Each point forms a new line. Then the points in $\sigma_{\text{term}} - 1$ are examined and matched with the points in σ_{term} based on the shortest distance. Any unmatched point in $\sigma_{\text{term}} - 1$ forms a new extreme line. The procedure is repeated until $\sigma = 0$ is reached. Even though there are many points near $\sigma = 0$ and they are close to each other, they can always match up with the points at a higher smoothing level or they form a new line. With this procedure, the corresponding location at $\sigma = 0$ can always be discovered. Therefore, we define the *true* position of a segment $U = [t_1, t_2, t_3]$ at the smoothing level σ by its cover Γ_U, which specifies the corresponding position at the zero-scale as

$$\Gamma_U = [u_1, u_2], \tag{9}$$

where u_1 and u_2 are the path length variables for the beginning and ending positions of the segment. Furthermore, matching segments found in different scales can be done by comparing their corresponding covers. For any two segments U and V at the levels σ_U and σ_V, respectively, where $\sigma_U \neq \sigma_V$, segments U and V are considered the same segment if $\Gamma_U = \Gamma_V$.

Identifying the span of a segment in the smoothing scale axis reveals the evolution of the segment. There are two important properties for a segment evolution: the formation level and the smooth-out level. The formation level indicates when the segment first appears, i.e., the smallest σ for the segment, while the smooth-out level indicates when the segment is smoothed-out and disappears, i.e., the largest $\sigma + 1$ for the segment. For example, the indentation segment [B, C, D] emerges at $\sigma = 44$ in Fig. 6(b) when all nested smaller irregularities have been smoothed out, and it ends at $\sigma = 102$ when the convex curvature line D closes off at the top, point A_E.

2.4.5. Hierarchical structures for indentation/protrusion segments

The extended scale-space image not only illustrates the evolution of the indentation/protrusion segments; it also helps organize segments into a hierarchical structure. Because of the causality property of Gaussian smoothing (Lindeberg, 1994), segments are smoothed out in a 'proper' order: small ones disappear before larger ones. Now when some smaller segments are smoothed out, larger segments may emerge at the same locations. The larger segments are considered as the 'global' segments to the smaller 'local' ones. Hence, a hierarchical structure of indentation/protrusion segments is formed.

As illustrated by Fig. 4, indentation and protrusion segments may overlap at a smoothing level. To avoid the complexity of overlapping segments within a hierarchical structure, we divide indentation segments and protrusion segments into two separate hierarchies, which are constructed by examining the inclusion property of the segment covers. For a segment U with the cover $\Gamma_U = [u_1, u_2]$ and the smooth-out level σ_U and a segment V with the

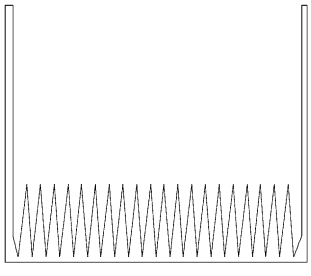

Fig. 7. The comb shape can cause self-intersection if the Gaussian smoothing process is not 'normalised' by its arc-length at each smoothing step.

cover $\Gamma_V = [v_1, v_2]$ and the smooth-out level σ_V, segment U is a local segment for the global segment V if $\sigma_U < \sigma_V$ and Γ_U is included inside Γ_V. The inclusion of Γ_U inside Γ_V, denoted by $\Gamma_U \subseteq \Gamma_V$, is expressed as

$$u_1 \geqslant v_1 \quad \text{and} \quad u_2 \leqslant v_2. \tag{10}$$

The segments U and V form a hierarchical tree structure because a global segment can nest one or more local segments. For instance, the indentation segments [B, C, D] and [D, K, L] are local indentation segments for the global segment [B1, C1, F] shown in Fig. 6(b). (These segments are also shown in Fig. 5 at $\sigma = 48$ and 102, respectively.)[3] By analysing the inclusion property of all indentation and protrusion segments, we obtain two hierarchical structures, one for indentation segments and the other for protrusion segments. Each hierarchical structure consists of a forest of tree structures, where the root of a tree structure is a global segment and its corresponding local segments are in the leaves of the tree.

Note that all contours are periodic. Special care has to be taken when a segment wraps around the beginning point of the parameterization process such as the indentation segment [H, I, J] shown in Fig. 6(b) (also in Fig. 5, $\sigma = 32$). The hierarchical relation between this segment and its local segments needed to be checked carefully.

2.4.6. Flat irregularity segments

As local segments smooth into global segments and the border turns into an oval shape, the overall curvature of the curve is reduced. Global segments tend to be flatter than their counter local segments. Without a restriction on the formation of a segment, sometimes a flat segment, which is a slightly bent indentation/protrusion segment, can be formed. This kind of flat segment often occurs near the root position of a tree structure in a segment hierarchy. For example, when the indentation segment [B, C, D] in Fig. 5 is smoothed out at $\sigma = 102$ and turns into a larger indentation segment [B1, C1, F], the new global segment [B1, C1, F] is a flat segment with a hardly noticeable indentation in the middle of the segment. (The indentation segments [B, C, D] and [B1, C1, F] are also labelled in the extended scale-space image in Fig. 6(b).) In order to control the formation of such a 'flat' irregularity segment, the three curvature extrema are checked at the formation level for every new segment $U = [t_1, t_2, t_3]$. If the absolute magnitude of the middle curvature extremum, t_2, or the maximum absolute magnitude of the first and the last curvature extrema, t_1, and t_3, are smaller than certain threshold and very close to zero, the newly formed segment is considered as an insignificant 'flat' indentation/protrusion segment. Mathematically, the criteria for a flat segment can be written as

$$|K(t_2)| < \varepsilon \quad \text{or} \quad \max\{|K(t_1)|, |K(t_3)|\} < \varepsilon, \tag{11}$$

where ϵ is the threshold, which is set to 0.01. All flat segments are removed from further computation.

In summary, by analyzing the extended scale-space image, we can track the evolution of all irregularity segments for the entire smoothing process. These segments may span multiple smoothing levels and they are organized separately in two hierarchical structures. Furthermore, the smooth-out level for each segment is an important piece of information that will be used in the computation of the border irregularity.

2.5. Calculate irregularity index

Each detected indentation/protrusion segment has an irregularity measure. From our sigma-ratio experiments, we learned that the measure should be area-based so that a *smaller* segment as shown in Fig. 3(a) has a proportional measure (based on area) to the *larger* segment shown in Fig. 3(b). An area-based measure also implies the method is stable for small changes (noise) along the border. Our approach is to observe the smoothing effect on the area of an indentation or a protrusion segment. When an indentation (or a protrusion) is smoothed-out, the indentation (or protrusion) is partially filled (or removed). For example, Fig. 8(a) shows a lesion border and the smoothed contour at the smooth-out level for the largest indentation at the bottom of the figure. The shaded area indicates the filling done by the smoothing process. (Likewise, Fig. 8(b) shows the same lesion border and the smoothed border for the most prominent protrusion at the bottom of the border. The shaded area represents the area removed by the smoothing process.) The size of the filled (or removed) area, termed

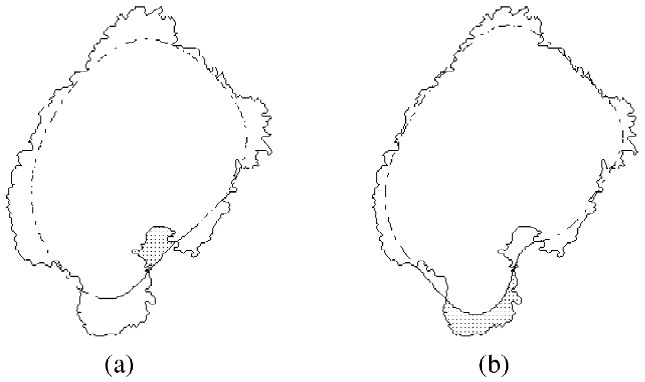

Fig. 8. Smoothing effect on indentation and protrusion. (a) A lesion border is shown by the solid line, while the smoothed curve corresponding to the smooth-out σ level for the largest indentation is shown by the dashed line. The shaded area denotes the irregularity area filled by the smoothing process. (b) The smoothed curve corresponding to the smooth-out σ level for the largest protrusion is shown by the dashed line. The irregularity area removed by the smoothing process is marked by the shaded area.

[3] Actually, the indentation segment [D, K L] is best illustrated at $\sigma = 32$ as it is almost smoothed out at $\sigma = 48$.

irregularity area, is used to determine the irregularity index.

The index for an indentation/protrusion segment must be normalized so that it can be used for comparison among irregularities in different lesion borders. Normalization is achieved by dividing the irregularity area by the smoothed contour at the corresponding smooth-out level. Therefore, the irregularity index (II) of an indentation/protrusion segment U, denoted by I_U, is defined as

$$I_U = \frac{\Delta_U}{R_U} \times 100\%, \tag{12}$$

where Δ_U is the irregularity area for segment U and R_U is the area of the smoothed contour at the smooth-out level.

The hierarchical structures described in Section 2.4.5 organize all indentation and protrusion segments of the entire smoothing process into two forests of tree structures. In particular, the set of root segments in the tree structures of both hierarchies represents all global irregular segments, which fully describe the complexity of the lesion border. Let us assume the root segments are $U_1, U_2, \ldots, U_n$. Their corresponding IIs, denoted by $I_1, I_2, \ldots, I_n$ respectively, provide a rich set of descriptions of the border. From this set of indices, many important parameters about a lesion border can be inferred. In particular, two important descriptors, the most significant irregularity index (MSII) and the overall irregularity index (OII), can be derived. The MSII of a lesion border L ranks all individual indices and indicates the largest indentation/protrusion segment of the border,

$$\text{MSII} = \max\{I_1, I_2, \ldots, I_n\}. \tag{13}$$

The OII represents the entire lesion shape, and is calculated by summing up all individual indices as

$$\text{OII} = \sum_{j=1}^{n} I_j. \tag{14}$$

Fig. 9 plots ten largest indentation/protrusion segments for the lesion border C shown in Fig. 2. The segments are sorted by their corresponding II. The top left-hand subfigure depicts the largest irregularity segment, a protrusion, with MSII = 4.2, while the next subfigure illustrates the largest indentation segment with an index of 2.4. Note that the indentation segment overlaps partially with the largest protrusion segment of the border. The third largest irregularity segment is another protrusion with an index of 1.9. The OII for this lesion border is 15.1.

3. User study

We designed a user study to test the new measures, the MSII and OII, with other common shape descriptors, namely the CI, FD and SFD, using 40 lesion borders which were selected from our pigmented lesion image database. These tested measurements were compared statistically with 14 dermatologists' clinical evaluations.

3.1. Method

3.1.1. Preparation of test data

The 40 pigmented lesions were selected from our skin image database, which was collected from patients who were referred to the Pigmented Lesion Clinics of the Division of Dermatology in Vancouver, BC, Canada. Before the colour images could be used for the study, they were pre-processed by two automatic programs as described in Section 2.1. The extracted lesion border for the 40 lesions are shown in Fig. 10.

3.1.2. Compactness index

The CI for these 40 lesion borders was computed according to the equation

$$\text{CI} = \frac{4\pi P^2}{A}, \tag{15}$$

where P is the perimeter of the border and A is the corresponding area.

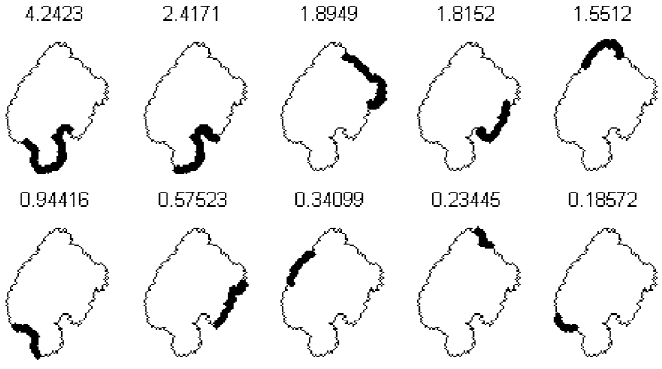

Fig. 9. Indentation/protrusion segments. Ten largest global indentation and protrusion segments for the lesion border C of Fig. 2 are plotted. The segments are sorted by their irregularity indices, which are shown at the top of each subfigure.

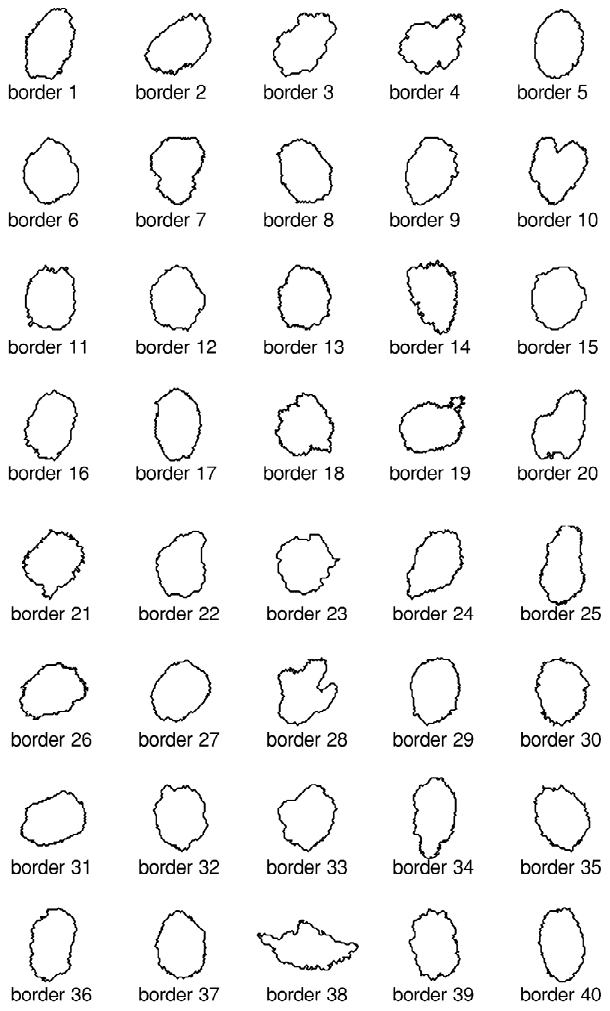

Fig. 10. Forty tested lesion borders.

3.1.3. Fractal dimension

The FD of a lesion border L, denoted by D, was estimated using the box counting method (Chaudhuri and Sarkar, 1995; Ng and Lee, 1996), which counted the number of boxes required to cover the border L. Various sizes of $r \times r$ grids (boxes) were placed over the lesion and the number of grids containing the border, $N(r)$, was counted. The relationship between $N(r)$ and D can be expressed as

$$N(r) = \lambda r^{-D}, \tag{16}$$

Expanding the equation, we have

$$\log\frac{1}{N(r)} = D \times \log(r) - \log(\lambda), \tag{17}$$

where λ is a constant. Thus, D is the slope of the linear Eq. (17), which can be computed by the least square fitting of the $\log(1/N(r))$ versus $\log(r)$ plot. (Fig. 11 shows the log–log plot for the lesion border C of Fig. 2.)

As mentioned in Section 1.2, Claridge et al. (1992) recognized that there were two types of fractal dimensions, structure and texture fractal dimension, associated with a lesion border. Furthermore, the SFD had a higher correlation with melanomas. When we examined the log–log plots for the fractal dimension (see Fig. 11 as an example for the log–log plot), we found that there was evidence to support the idea of two fractals. The breakpoint for these two fractals was estimated to be located between the fourth and fifth data points in the log–log plot. Therefore, we divided the data points at the breakpoint and used the upper half of data, from the fifth data point, to compute the SFD of the lesion border.[4]

3.1.4. Irregularity index

The methodological development described in Section 2 has been implemented in Matlab, running on a Pentium 700 MHz computer. The computation is extensive while no optimization has yet been implemented. The execution time usually takes less than a minute, depending on the border length. For each tested lesion border, the MSII and OII were computed.

3.1.5. Clinical evaluation

Fourteen experienced dermatologists were asked to visually evaluate the 40 tested lesion borders using a scale of 1 to 4. The scale 1 denoted the most benign looking lesion border, while the scale 4 denoted a border which has the highest probability of being a melanoma. A user study package was prepared by plotting the lesion borders into 4 pages, 10 borders per page. Because the size of a lesion is itself a marker of risks, all lesion sizes were standardized to an equal area so that the evaluation was based solely on the border features. To avoid all lesion borders with high (or low) OII values clustering into one page, the following placement scheme was employed. The four lesion borders associated with the highest OII values were placed separately, one in a page. The rest of the 36 lesion borders were divided into 4 groups according to their OII values and each group was randomized and distributed evenly in the four pages. Furthermore, within a page, the placement of a lesion border was randomized. The dermatologists were informed only that there was at least one border in the scale category 1 and at least one border in the scale category 4 in each page. However, the number of lesions in each of the 4 scale categories in a page and in the entire study was not mentioned. The dermatologists could freely assign a lesion border into any scale category and any number of borders into a category. A user consent form

[4] We tested our implementation of FD and SFD using a circle, a Koch snowflake and a Koch square flake, whose theoretical fractal dimensions are 1, 1.262 and 1.5, respectively (Peitgen et al., 1992). The computed FD values for the above objects were 0.985 (1.5% error), 1.286 (1.9% error) and 1.502 (0.13% error), respectively. Although the SFD uses only the upper half of data points for estimation, the computation was stable and the corresponding values were 1.051 (5.1% error), 1.293 (2.46% error) and 1.500 (0% error).

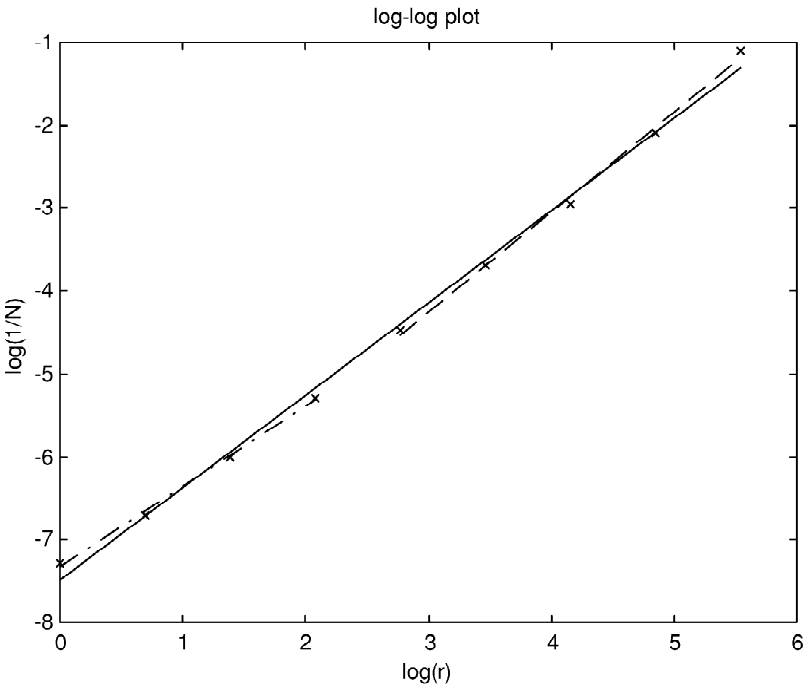

Fig. 11. The log–log plot of the fractal dimension. This plot is constructed using the lesion border C in Fig. 2. The fractal dimension is the slope of the solid line, which is estimated by all the data points. The structure fractal dimension is the slope of the dashed line (–), which is estimated by the fifth to the ninth data points. The fractal dimension for this lesion border is 1.115, while the structure fractal dimension is 1.207.

and an information sheet were also included in the package. The information sheet described the study and provided evaluation instructions. The dermatologists were asked to read over the instructions and complete the evaluation. Other than the study package, there was no further communication with the dermatologists.

This was a double-blinded test because all program development and calculations were done before the clinical evaluation and the dermatologists did not know the results of the tested measurements prior to the evaluation. The computed measurements were then compared statistically against the average dermatologists' evaluation, which was considered as the gold standard.

3.1.6. Statistical methods

The user study results were tested by statistical methods using SPSS. First the Kendall *W*, the coefficient of concordance, was computed for the dermatologists' evaluation to ensure a reasonable agreement among the dermatologists so that the gold standard can be formed. The value of *W* ranges from 0 to 1, where 0 implies there is no agreement among the dermatologists and 1 implies a perfect agreement (Norusis, 1988). The gold standard was obtained by averaging the clinical evaluation for each tested lesion. Because we have to compare the gold standard and the computed measures, which were in different scales, we selected the Spearman's rank correlation to determine the correlation coefficient for each pair of measurements, the average clinical evaluation, CI, FD, SFD, OII and MSII. Based on the rank of the measure, the Spearman coefficient can properly determine the correlation between measures of different scales. Its value ranges from -1 to $+1$, where -1 ($+1$) implies a perfect negative (positive) correlation between the rank of two measurements, and 0 implies there is no linear correlation between the rank of two measurements (Norusis, 1988)

4. Results and discussion

4.1. Results

The clinical evaluation results of 14 dermatologists are reported in columns 'C1' to 'C14' in Table 1. The coefficient of concordance, Kendall *W*, for all 14 clinical evaluations was then determined as $W = 0.77$ ($p = 0.00$). The clinical evaluations were averaged for each lesion border and listed in column 'Avg' of Table 2. The tested measurements (CI, FD, SFD, OII and MSII) were also computed and presented in Table 2. The most significant indentation/protrusion segment for each tested border is plotted in Fig. 12. The Spearman coefficients, shown in the second column of Table 3, were calculated for each pair of the average clinical evaluation and the tested measurement. Furthermore, to expose the relationship between the average clinical evaluation and the tested measurements, we plot the average clinical evaluation against each tested measurement separately in Fig. 13.

Table 1
Clinical evaluation of the lesion borders shown in Fig. 10 for all fourteen experienced dermatologists

Border	C1	C2	C3	C4	C5	C6	C7	C8	C9	C10	C11	C12	C13	C14
1	2	1	2	1	2	2	2	1	1	1	2	1	2	2
2	3	2	2	1	2	2	2	1	1	1	2	2	3	2
3	2	3	4	2	3	3	2	2	3	3	3	3	4	3
4	4	4	3	4	4	4	4	3	4	4	4	4	4	4
5	1	1	1	1	1	1	1	1	1	1	1	1	1	1
6	1	1	2	1	2	2	2	2	1	1	2	1	2	2
7	3	3	4	4	4	3	3	3	3	2	3	3	4	2
8	2	1	1	1	2	2	2	1	1	1	1	1	1	1
9	3	2	3	3	3	2	2	2	2	2	2	2	3	1
10	3	4	4	4	4	4	3	4	3	4	3	3	4	3
11	2	2	3	1	2	2	2	1	1	2	1	1	3	1
12	1	1	2	1	2	2	2	1	1	1	2	1	1	1
13	2	3	2	1	2	2	1	2	2	2	2	2	2	1
14	3	3	2	2	3	3	2	3	2	3	2	4	3	2
15	1	1	3	1	1	1	2	1	1	1	1	1	2	1
16	1	2	2	2	2	2	2	1	1	1	1	2	1	1
17	2	1	1	1	1	1	2	1	1	1	1	1	1	1
18	4	4	4	3	4	3	3	3	3	4	3	4	4	4
19	4	4	4	4	4	3	4	4	4	4	4	4	4	2
20	2	3	4	4	4	4	3	3	2	3	3	3	4	3
21	3	4	4	3	3	3	3	3	3	4	4	3	4	2
22	1	2	2	1	3	2	2	2	2	2	2	2	2	2
23	2	3	3	2	2	2	2	3	2	3	3	3	4	2
24	1	2	3	2	3	2	3	2	1	2	2	3	2	3
25	2	1	2	1	2	3	2	2	1	2	2	3	2	3
26	3	2	2	1	2	2	2	2	1	2	2	2	1	1
27	2	1	2	1	2	1	2	1	1	1	1	1	1	1
28	4	4	4	4	4	4	4	4	4	4	4	4	4	4
29	1	1	1	1	1	2	1	1	1	1	1	1	1	1
30	3	2	2	1	2	2	2	2	1	2	2	1	2	1
31	1	1	3	1	2	1	2	1	1	2	2	1	1	1
32	1	3	4	2	2	1	3	2	2	3	2	2	3	2
33	2	3	3	2	3	1	3	2	2	2	2	2	3	2
34	3	3	4	2	3	2	3	2	2	3	3	3	4	3
35	2	2	2	1	2	1	2	1	2	2	1	2	2	1
36	2	2	2	1	1	2	2	1	1	2	1	2	1	1
37	1	1	2	1	1	1	1	1	1	1	1	1	1	1
38	4	4	4	4	4	4	4	4	4	4	4	4	4	4
39	2	3	3	2	2	3	2	3	2	2	2	3	4	2
40	1	1	1	1	1	2	2	1	1	2	1	1	1	1

4.2. Discussion

Clinical evaluation of border irregularity is a difficult task for dermatologists as they are trained to diagnose pigmented skin lesions using not only border features, but also other symptoms. Even experienced dermatologists have difficulty to interpret the lesion border as the sole feature. Claridge et al. (1998) reported a low agreement (coefficient of concordance $W = 0.47$) among 20 clinicians, when they were asked to sort 20 lesion borders contours in the order of increasing border irregularity. Such a low agreement casts a doubt on the possibility of forming a valid gold standard. Therefore, forming the gold standard becomes an issue.

In order to achieve a reliable gold standard for our user study, we asked dermatologists to classify a lesion border outline into a small score scale, ranging from 1 to 4. Other than the most benign looking contour group (score value 1) and the most malignant looking contour group (score value 4), there were only two intermediate groups. Dermatologists could confidently assign a score value to a tested lesion border based on their own subjective cut points between groups. Judging from the clinical evaluation results in Table 1, this score scale worked well and the fourteen dermatologists achieved a good agreement. Among the 40 lesion borders, 32 of them had a majority agreement, i.e. agreed by at least 8 dermatologists. More importantly, 39 lesion borders had the scores difference at most by 2. This implied that the dermatologists' cut points were *close* to each other. The high Kendall W statistic, $W = 0.77$ ($p = 0.00$), further confirmed the good agreement among the clinical evaluations. With the assurance of a good agreement, we set up the gold standard by averaging the clinical evaluations for each lesion border.

Table 2
Average clinical evaluation and tested measurements for lesion borders shown in Fig. 10

Border	Avg	CI	FD	SFD	OII	MSII	Histology
1	1.6	3.44	1.184	1.349	5.7	1.1	–
2	1.9	3.75	1.117	1.217	5.5	0.6	–
3	2.9	2.30	1.080	1.202	8.7	1.4	–
4	3.9	3.44	1.118	1.208	17.1	3.2	Melanoma
5	1.0	1.69	1.096	1.236	2.8	0.4	–
6	1.6	1.90	1.092	1.256	3.5	0.4	Melanoma
7	3.1	3.72	1.153	1.242	5.4	1.1	–
8	1.3	3.07	1.101	1.124	3.4	0.2	–
9	2.3	2.13	1.083	1.224	5.7	1.0	–
10	3.6	3.90	1.126	1.247	8.2	2.2	–
11	1.7	2.32	1.083	1.124	5.1	0.7	–
12	1.4	2.05	1.081	1.183	5.2	1.3	–
13	1.9	3.19	1.128	1.221	5.0	0.7	–
14	2.6	4.95	1.176	1.284	9.4	1.4	–
15	1.3	1.49	1.110	1.404	3.4	0.8	–
16	1.5	2.26	1.112	1.264	5.7	1.7	–
17	1.1	3.02	1.183	1.348	3.3	0.3	–
18	3.6	4.50	1.131	1.216	8.4	1.5	–
19	3.8	6.18	1.181	1.245	10.8	3.6	–
20	3.2	2.81	1.118	1.230	9.2	2.8	–
21	3.3	4.22	1.127	1.148	8.9	1.5	–
22	1.9	1.93	1.089	1.350	5.7	1.3	–
23	2.6	1.91	1.112	1.585	9.0	2.2	–
24	2.2	3.49	1.106	1.176	5.1	0.5	–
25	2.0	3.52	1.161	1.301	5.3	0.6	–
26	1.8	3.91	1.117	1.180	5.7	0.5	–
27	1.3	2.42	1.085	1.154	3.0	0.4	–
28	4.0	3.43	1.123	1.298	22.7	7.2	Melanoma
29	1.1	2.77	1.076	1.100	3.5	0.3	–
30	1.8	3.43	1.163	1.263	5.1	0.7	–
31	1.4	2.63	1.094	1.179	3.4	0.6	–
32	2.3	1.75	1.063	1.230	5.6	1.3	Melanoma
33	2.3	2.05	1.076	1.213	8.4	2.4	–
34	2.9	3.12	1.135	1.240	8.3	3.0	–
35	1.6	2.60	1.110	1.183	5.5	0.5	–
36	1.5	2.39	1.170	1.447	5.4	0.9	–
37	1.1	2.53	1.146	1.322	3.5	0.6	–
38	4.0	5.39	1.124	1.243	18.9	4.1	–
39	2.5	2.68	1.141	1.296	8.3	1.1	–
40	1.2	2.61	1.147	1.291	3.1	0.5	–

In Fig. 13, the plots of the tested measurements against the average clinical evaluation showed that no tested measurement achieved a perfect correlation with the gold standard. However, the OII and MSII had a better linear relationship with the average clinical evaluation than the other three tested measurements. Similarly, from the Spearman coefficients (Table 3), the OII had the highest correlation coefficient, 0.88, against the clinical evaluation. The closest second was the MSII, 0.81. The CI, FD and SFD achieved much lower correlation coefficients, 0.51, 0.19 and 0.00, respectively. These three measures had problems in detecting large structure indentations and protrusions. For example, they failed to properly measure the prominent structure irregularities in the tested border 28 (CI = 3.43, FD = 1.12, SFD = 1.30). These three tested measurements were very close to the border 40 (CI = 2.61, FD = 1.15, SFD = 1.29), which had no structure irregularity, but only texture irregularities. Furthermore, it was surprising to discover that the SFD performed poorer than the FD. The SFDs of lesion border 5 (1.24), border 6 (1.26), border 15 (1.40), border 17 (1.35), border 37 (1.32) and border 40 (1.29) were too high for the benign looking borders in the test set. The problem was caused by applying a wrong model to a border that had only small texture variations. This type of border should have only one overall fractal dimension. When the data points of the log–log plot were separated into two groups, the SFD estimation was incorrect due to the misplacement of the breakpoint. Removing these six lesion borders, the Spearman's coefficient for the SFD and the average clinical evaluation improved to 0.31.

According to Fig. 13, there are some outliers, three in the overall irregularity index subfigure, one in the most significant irregularity index subfigure and one in the

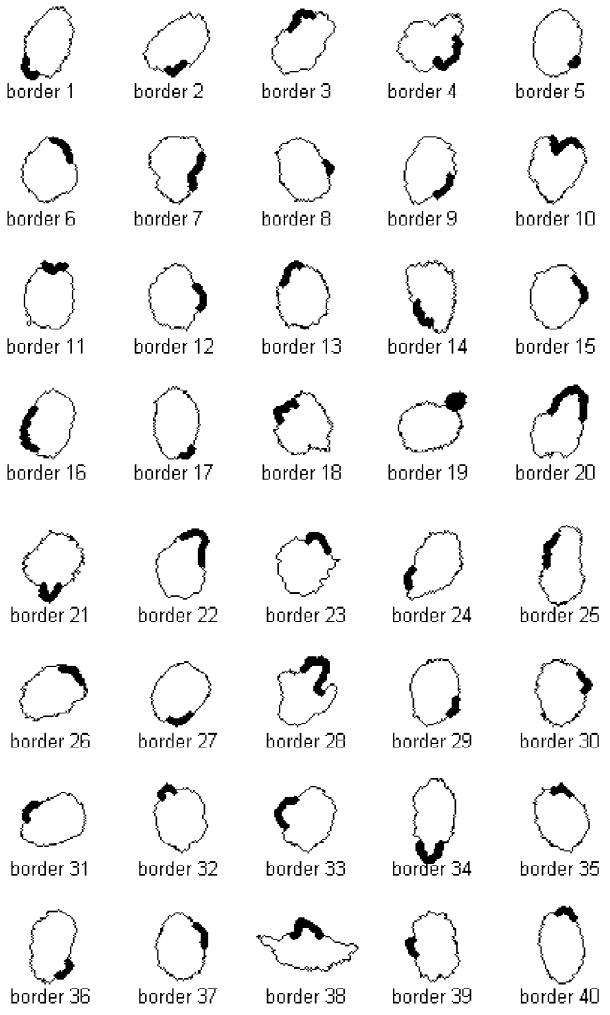

Fig. 12. The most significant indentation/protrusion segment of the tested lesion borders. The corresponding Most Significant Irregularity Index is listed in Table 2.

structure fractal dimension subfigure. These outliers (borders 4, 19, 23 and 28) were actually caused by the high response of the overall irregularity index, most significant irregularity index and structure fractal dimension to the most irregular borders. Although Spearman's coefficient is based on the rank of the measure and is not affected by the outliers, we repeated the Spearman's coefficient analysis with the outliers removed. The results are listed in the last column of Table 3 and shows there was no significant change from the analysis using all the borders.

The CI and FD are well-known shape descriptors for the overall border roughness. Both methods compute a single point estimation without actually identifying the indentations and protrusions on the lesion border. A higher value implies a rougher border with the existence of indentations and protrusions. However, a single point estimation can be easily skewed if the variance of the border ruggedness is large. For example, a lesion with a large protrusion on a relatively smooth border, such as lesion border 20, may have the single point estimation dampened by the smoothed portion. Its low responses for the CI (2.81) and FD (1.12) were mainly caused by the smooth border that had few texture irregularities.

On the other hand, our method of measuring the II identifies all indentations and protrusions on the lesion border. Because each irregularity is carefully analyzed independently, this method not only returns a more accurate overall measurement, which represents the roughness for the entire border, but also gives a set of measurements for all global irregularities (see Fig. 9) that fully describes the complexity of the lesion border. In particular, combining the OII and MSII may deduce many interesting properties of the lesion borders. For example, the OII (5.5) and MSII (0.5) of lesion border 35 indicated that it had no structure irregularity, but a lot of texture irregularities. A similar situation holds for lesion border 2 (OII = 5.5, MSII = 0.6). However, lesion border 32 with OII = 5.6 and MSII = 1.3 implied that the lesion border had a larger irregularity, but less texture irregularities than lesion borders 35 and 2. On the other hand, the OII (22.7) and MSII (7.2) for lesion border 28 suggested the border had some major indentations and protrusions. Furthermore, the rich set of measurements for the global irregularities can be used to infer other border properties such as enumerating the number of *large* or *medium* irregularities.

Our new area-based method overcomes the non-linearity and the long-and-narrow indentation problems with our earlier SR method. For example, the MSII and OII for the phantom in Fig. 14(a) are 0.3 and 0.4, respectively.[5] They differ significantly from the MSII (7.4) and OII (7.5) for the phantom in Fig. 14(b). The small MSII for Fig. 14(a) reflect the small area of the indentation and imply that the new algorithm is less sensitive to the hair problem.

[5]The small texture irregularity, 0.1, is due to discretization error.

Table 3
Spearman coefficients for the average clinical evaluation and tested measurements

	Average clinical evaluation for all lesion borders	Average clinical evaluation with outliers removed
Compactness Index (CI)	0.51	0.49
Fractal Dimension (FD)	0.19	0.16
Structure Fractal Dimension (SFD)	0.00	−0.06
Overall Irregularity Index (OII)	0.88	0.85
Most Significant Irregularity Index (MSII)	0.81	0.76

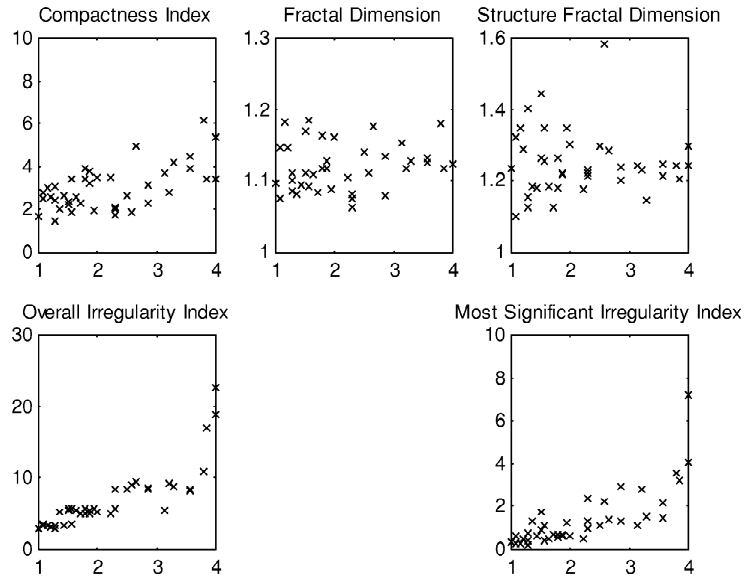

Fig. 13. Plotting the tested measurements (Compactness Index, Structure Fractal Dimension, Overall Irregularity Index and Most Significant Irregularity Index) against the average clinical evaluation separately. The average clinical evaluation is in the *x*-axis, while the tested measurement is in the *y*-axis.

Missing a hair by the preprocessor DullRazor or a small change on the border does not cause a large change in values for MSII and OII.

Another advantage of obtaining this set of measurements is that the algorithm can pinpoint and highlight a potential problematic area, such as the most significant irregular segments, and can explain the OII by its individual sub-components. Therefore, physicians can verify the highlighted irregular segments and their indices before making the final diagnosis. The detailed information provided by the new indices may be useful for a computer-aided diagnostic device.

4.3. Overall irregularity index and histology

One of the considerations for designing the user study was the gold standard selection for the validation process. Should it be the clinical evaluation or histology status? Because border irregularity is a clinical diagnosis feature defined by dermatologists, making dermatologist's clinical evaluation as the gold standard was the most appropriate choice. In other words, when dermatologists had concerns on an irregular border, the new measures should similarly reflect these concerns. A computer program encoding such knowledge could be used by other non-dermatologists such as health practitioners or the general public. Also it could be used as an objective alternative for dermatologists.

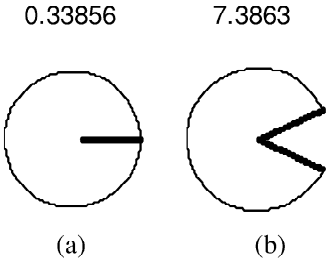

Fig. 14. The most significant indentations for the phantoms showed in Fig. 3 are highlighted. The associated MSII is shown at the top of each phantom.

In spite of the above philosophical arguments, it is interesting to compare the new measures, in particular the OII, with the histological results of the lesions. Unfortunately, our data were not optimized for the histological analysis because there were only 4 melanomas based on histological reports. (The 4 melanomas corresponded to lesion borders 4, 6, 28 and 32 of Fig. 10 and Table 2). The other 36 lesions were non-melanomas. Furthermore, the histology analyses were performed by different hospitals over a lengthy period.

To assess the discriminatory power of the OII, we had to classify the lesions into melanoma and non-melanoma groups based on the OII values. The selection of a classification method became critical. A simple objective classification method assumes all melanomas would have most irregular border and all non-melanomas would have most regular border (Claridge et al., 1992). Therefore, the 4 lesions with the highest OII values (lesion borders 28, 38, 4 and 19 in Table 2) were classified as melanomas and all other lesions were classified as non-melanomas. With this classification method for melanomas, there were 2 true positives, 2 false positives, 34 true negatives and 2 false negatives. The sensitivity of detecting melanomas (Grin et al., 1990) was determined as 50% and the specificity of detecting melanomas (Grin et al., 1990) was determined as 94%.

The above discriminatory analysis suggested that border shape information had excellent power to screen out non-

melanomas, but moderate power to detect melanomas. The analysis result confirmed our knowledge that melanomas cannot be diagnosed properly by a single clinical feature. In particular, some melanomas may have regular borders and some non-melanomas may have irregular borders. Based on a sole clinical feature, there is a high probability of misclassification. To properly diagnose melanomas, we have to incorporate the OII with other melanoma features in a classifier.

In order to verify the actual performance of the OII, we also need to compare the average clinical evaluations and the histological results (Table 2). Once again, the simple objective classification method was applied. The average clinical evaluations were ranked and the 4 lesions with the highest scores (lesion border 28, 38, 4 and 19) were classified as melanomas and the rest as non-melanomas. With this classification method, we found that the 40 lesions were classified the same as the OII classification method, i.e., the same 4 lesions were classified as melanomas and the same 36 lesions were classified as non-melanomas. The dermatologists would misclassify the same two pathological melanomas as non-melanomas (false negative) and the same two pathological non-melanomas as melanomas (false positive). Therefore, we confirmed that our algorithm indeed captured the knowledge of expert dermatologists on analysing border shape.

5. Conclusion and future work

We have designed and implemented a new measure called the *irregularity index* (II) for estimating the border irregularity of melanocytic lesions. The advantage of the new measure is that it directly locates indentations and protrusions along the lesion border. Extending scale-space images to analyse curve segments, we enumerate all global irregular segments and compute their associated indices. This set of measurements provides a rich description for the lesion border that is sensitive to structure irregularities. We further examined two measurements derived from the set, the OII and MSII, and compared them with other common shape descriptors, namely, the CI, FD and SFD. In a double-blinded user study with 40 lesion borders and 14 dermatologists, we discovered that our new indices had the highest correlation with clinical evaluations. The algorithm seemed to capture the knowledge of expert dermatologists in evaluating lesion border. In future work, we will investigate the full potential and stability of the II in a larger study with more observers.

Acknowledgements

The authors thank Dr. Chantal Bolduc, Dr. Richard Crawford, Dr. William Danby, Dr. Anne Davis, Dr. Brian Gregory, Dr. Vincent Ho, Dr. Harvey Liu, Dr. Lynette Margesson, Dr. Francisco Paschoal, Dr. Jason Rivers, Dr. Jerry Shapiro, Dr. Cecil Sigal, and Dr. David Zloty for their assistance in evaluation the lesion borders and Dr. Andy Coldman and Dr. John Spinelli for their advice on the statistical analysis of the experiment data. Furthermore, this work was supported in part by a BC Health Research Foundation grant #142(97-2).

Appendix A. Classic and extended curvature scale-space images

The classic and the extended curvature scale-space images form a dual space because these two images are constructed by different feature points of the smoothed borders. In Appendix A, we state the parallel mathematical properties and the differences for these two images. The proofs of the properties have been published elsewhere (Lee et al., 2001).

Property 1(a). *In classic curvature scale-space images, the apex of a contour arc is the point* (τ, ξ) *such that* $K(\tau, \xi) = 0$ *and* $\partial K(\tau, \xi)/\partial t = 0$.

Property 1(b). *In extended curvature scale-space images, the apex of a contour arc is the point* (τ, ξ) *such that* $\partial K(\tau, \xi)/\partial t = 0$ *and* $\partial^2 K(\tau, \xi)/\partial t^2 = 0$.

Property 2(a). *In classic curvature scale-space images, excluding the apex point, one side of a contour arc has the property* $\partial K/\partial t > 0$ *and the other side of the contour arc has the property* $\partial K/\partial t < 0$.

Property 2(b). *In extended curvature scale-space images, excluding the apex point, one side of a contour arc has the property* $\partial^2 K/\partial t^2 > 0$ *and the other side of the contour arc has the property* $\partial^2 K/\partial t^2 < 0$.

Property 3. *In the contours of an extended curvature scale-space image, the points where the concave extrema and convex extrema meet are the zero curvature points.*

Property 4(a). *In classic curvature scale-space images, all curvature zero-crossings disappear at* σ_{term}.

Property 4(b). *In extended curvature scale-space images, all curvature extrema may disappear (a special case of a circle) or at least 4 curvature extrema remain at* σ_{term}.

References

Armstrong, B.K., English, D.R., 1996. Cutaneous malignant melanoma. In: Schottenfeld, D., Fraumeni, Jr. J.F. (Eds.), Cancer Epidemiology and Prevention. Oxford University Press, New York, pp. 1282–1312.

Asada, H., Brady, M., 1983. The curvature primal sketch. IEEE Trans. PAMI 8, 2–14.

Attneave, F., 1954. Some informational aspects of visual perception. Psychol. Rev. 61, 183–193.

Balch, C.M., Houghton, A., Peters, L., 1989. Cutaneous melanoma. In: DeVita, Jr. V.T., Hellman, S., Rosenberg, S.A. (Eds.), Cancer Principles and Practice of Oncology. J.B. Lippincot Company, Philadelphia, pp. 1499–1542.

Binder, M., Steiner, A., Schwarz, M., Knollimayer, S., Wolff, K., Pehamberger, H., 1994. Application of an artificial neural network in epiluminescence microscopy pattern analysis of pigmented skin lesions: A pilot study. Br. J. Dermatol. 130, 460–465.

Bono, A., Tomatis, S., Bartoli, C., Tragni, G., Radaelli, G., Maurichi, A., Marchesini, R., 1999. The ABCD system of melanoma detection: A spectrophotometric analysis of the asymmetry, border, color, and dimension. Cancer 85 (1), 72–77.

Caldwell, B.C., Stapleton, S.J., Holdsworth, D.W., Jong, R.A., Weiser, W.J., Cooke, G., Yaffe, M.J., 1990. Characterisation of mammographic parenchymal pattern by fractal dimension. Phys. Med. Biol. 35, 235–247.

Cascinelli, N., Ferrario, M., Tonelli, T., Leo, E., 1987. A possible new tool for clinical diagnosis of melanoma: the computer. Clinical Diagnosis of Melanoma 16 (2), 361–367.

Chaudhuri, B.B., Sarkar, N., 1995. Texture segmentation using fractal dimension. IEEE Trans. PAMI 17, 72–77.

Claridge, E., Hall, P.N., Keefe, M., Allen, J.P., 1992. Shape analysis for classification of malignant melanoma. J. Biomed. Eng. 14, 229–234.

Claridge, E., Morris-Smoth, J.D., Hall, P.N., 1998. Evaluation of border irregularity in pigmented skin lesions against a consensus of expert clinicians. In: Medical Image Understanding and Analysis, Leeds, UK.

Colot, O., Devinoy, R., Sombo, A., de Brucq, D., 1998. A color image processing method for melanoma detection. In: Proceedings of the First International Medical Imaging Computing and Computer-Assisted Intervention. Cambridge, pp. 562–569.

Cotton, S., Claridge, E., Hall, P., 1999. A skin imaging method based on a colour formation model and its application to the diagnosis of pigmented skin lesions. In: Proceedings of Medical Image Understanding and Analysis. Oxford, pp. 49–52.

Elbaum, M., 2000. A unique multispectral digital dermoscope for diagnosis of early melanoma. The Melanoma Letter 18 (1), 4–5.

Ercal, F., Chawla, A., Stoecker, W.V., Lee, H.C., Moss, R., 1994. Neural network diagnosis of malignant melanoma from color images. IEEE Trans. Biomed. Eng. 41, 837–845.

Fleming, M.G., 2000. Image analysis for melanoma diagnosis. The Melanoma Letter 18 (1), 1–3.

Gage, M., Hamilton, R.S., 1986. The heat equation shrinking convex plane curves. J. Differential Geometry 23, 69–96.

Golston, J.E., Stoecker, W.V., Moss, R.H., Dhillon, I.P.S., 1992. Automatic detection of irregular borders in melanoma and other skin tumors. Computerized Medical Imaging and Graphics 16, 199–203.

Grayson, M., 1987. The heat equation shrinks embedded plane curves to round points. J. Differential Geometry 26, 285–314.

Greenspan, H.P., Benney, D.J., 1973. Calculus – An Introduction to Applied Mathematics. McGraw Hill.

Grin, C.M., Kopf, A., Welkovich, B., Bart, R., Levenstein, M., 1990. Accuracy in the clinical diagnosis of malignant melanoma. Archives Dermatol. 126, 763–766.

Gutkowicz-Krusin, D., Elbaum, M., Szwaykowski, P., Kopf, A.W., 1997. Can early malignant melanoma be differentiated from atypical melanocytic nevus by in vivo techniques? Skin Research and Technology 3, 15–22.

Hall, P.N., Claridge, E., Morris, J.D., 1995. Computer screening for early detection of melanoma – is there a future? Br. J. Dermatol. 132, 325–338.

Hoffman, D.D., Richards, W.A., 1985. Parts of recognition. Cognition 18, 65–96.

Keefe, M., Dick, D., Wakeel, R., 1990. A study of the value of the seven-point checklist in distinguishing benign pigmented lesions from melanoma. Clinical Experimental Dermatol. 15, 167–171.

Lee, T., Ng, V., McLean, D., Coldman, A., Gallagher, R., Sale, J., 1995. A multi-stage segmentation method for images of skin lesions. In: Proceedings of IEEE Pacific Rim Conference on Communications, Computers and Signal Processing, Victoria, British Columbia, pp. 602–605.

Lee, T., Ng, V., Gallagher, R., Coldman, A., McLean, D., 1997. DullRazor: A software approach to hair removal from images. Comput. Biol. and Med. 27, 533–543.

Lee, T., Atkins, S., Gallagher, R., MacAulay, C., Coldman, A., McLean, D., 1999. Describing the structural shape of melanocytic lesions. In: Image Processing, Proc. SPIE, San Diego, Vol. 3661, pp. 1170–1179.

Lee, T.K., Atkins, M.S., Li, Z.-N., 2001. Indentations and protrusion detection and its applications. In: Kerckhove, M. (Ed.), Proceedings of the Third International Conference on Scale Space and Morphology in Computer Vision. Springer, Vancouver, Canada, pp. 335–343.

Lindeberg, T., 1993. Effective scale: A natural unit for measuring scale-space lifetime. IEEE Trans. PAMI 15, 1068–1074.

Lindeberg, T., 1994. Scale-space Theory in Computer Vision. Kluwer Academic Publishers, Boston.

MacAulay, C.E., 1989. Development, implementation and evaluation of segmentation algorithms for the automatic classification of cervical cells. Ph.D. thesis, University of British Columbia.

Maize, J.C., Ackerman, A.B., 1987. Pigmented Lesions of the Skin. Lea & Febiger, Philadelphia.

Mandelbrot, B.B., 1982. The Fractal Geometry of Nature. W.H. Freeman and Co, New York.

Menzies, S.W., Crook, B., McCarthy, W.H., Bischof, L., Talbot, H., Breen, E., Stone, G., Chan, D., Gutenev, A., Thompson, R.L., Bourloutski, G., Skladnev, V.N., 1997. Automated instrumentation for the diagnosis of invasive melanoma. Skin Research and Technology 3 (3), 200.

Mokhtarian, F., Mackworth, A., 1986. Scale-based description and recognition of planar curves and two-dimensional shapes. IEEE Trans. PAMI 8, 34–43.

Mokhtarian, F., Mackworth, A., 1992. A theory of multiscale, curvature-based shape representation for planar curves. IEEE Trans. PAMI 14, 789–805.

Mokhtarian, F., Suomela, R., 1998. Robust image corner detection through curvature scale space. IEEE Trans. PAMI 20, 1376–1381.

Ng, V., Lee, T., 1996. Measuring border irregularities of skin lesions using fractal dimensions. In: SPIE Photonics China, Electronic Imaging and Multimedia Systems, Beijing, Vol. 2898, pp. 64–72.

Norusis, M.J., 1988. SPSS-X Introductory Statistics Guide for SPSS-X Release 3. SPSS Inc.

Peitgen, H.O., Jurgens, H., Saupe, D., 1992. Chaos and Fractals. Springer-Verlag, New York.

Pentland, A., 1984. Fractal-based description of natural scenes. IEEE Trans. PAMI 6, 661–674.

Richards, W., Hoffman, D.D., 1985. Condon constraints on closed 2D shapes. Computer Vision, Graphics, and Image Processing 31, 265–281.

Richards, W., Dawson, B., Whittington, D., 1986. Encoding contour shape by curvature extrema. J. Opt. Soc. Am. A 3 (9), 1483–1491.

Rivers, J.K., 1996. Melanoma. Lancet 347, 803–807.

Schindewolf, T., Stolz, W., Albert, R., Abmayr, W., Harms, H., 1992. Classification of melanocytic lesions with color and texture analysis using digital image processing. Analytical and Quantitative Cytology and Histology 15, 1–11.

Seidenari, S., Burroni, M., Giordana, D.E., Pepe, P., Belletti, B., 1995. Computerized evaluation of pigmented skin lesion images record by a videomicroscope: Comparison between polarizing mode observation and oil/slide mode observation. Skin Research and Technology 1, 187–191.

Siddiqi, K., Kimia, B.B., 1995. Parts of visual form: Computational aspects. IEEE Trans. PAMI. 17 (3), 239–251.

Stoecker, W.V., Moss, R.H., 1992. Editorial: digital imaging in dermatology. Computerized Medical Imaging and Graphics 16 (3), 145–150.

Stoecker, W.V., Moss, R., Ercal, F., Umbaugh, S., 1995. Nondermatoscopic digital imaging of pigmented lesions. Skin Research and Technology 1, 7–16.

ter Haar Romeny, B.M. (Ed.), 1994. Geometry-Driven Diffusion in Computer Vision. Kluwer Academic Publisher, Dordrecht, Boston, London.

White, R.G., Perednia, D.A., Schowengerdt, R.A., 1991. Automated feature detection in digital images of skin. Computer Methods and Programs in Biomedicine 34, 41–60.

White, R., Rigel, D.S., Friedman, R., 1992. Computer applications in the diagnosis and prognosis of malignant melanoma. Dermatologic Clinics 9, 695–702.

Witkin, A.P., 1983. Scale space filtering. In: Proceedings of the 8th International Joint Conference of Artificial Intelligent, pp. 1019–1022.